Available online at www.sciencedirect.com
SCIENCE DIRECT®
International Journal of Multiphase Flow 31 (2005) 1155–1180
International Journal of Multiphase Flow
www.elsevier.com/locate/ijmulflow

Relative permeability and capillary pressure functions of porous media as related to the displacement growth pattern

M.A. Theodoropoulou, V. Sygouni, V. Karoutsos, C.D. Tsakiroglou *

Institute of Chemical Engineering and High Temperature Chemical Processes—Foundation for Research and Technology Hellas, Stadiou Street, Platani, P.O. Box 1414, 26504 Patras, Greece

Received 14 October 2004; received in revised form 29 June 2005

Abstract

Visualization experiments of the unsteady immiscible displacement of a fluid by another are performed on glass-etched pore networks of well-controlled morphology by varying the fluid system and flow conditions. The measured transient responses of the fluid saturation and pressure drop across the porous medium are introduced into numerical solvers of the macroscopic two-phase flow equations to estimate the non-wetting phase, k_{rnw}, and wetting phase, k_{rw}, relative permeability curves and capillary pressure, P_c, curve. The correlation of k_{rnw}, k_{rw}, and P_c with the displacement growth pattern is investigated. Except for the capillary number, wettability, and viscosity ratio, the immiscible displacement growth pattern in a porous medium may be governed by the shear-thinning rheology of the injected or displaced fluid, and the porous sample length as compared to the thickness of the frontal region. The imbibition k_{rnw} increases as the flow pattern changes from compact displacement to viscous fingering or from viscous to capillary fingering. The imbibition k_{rw} increases as the flow pattern changes from compact displacement or capillary fingering to viscous fingering. As the shear-thinning behaviour of the NWP strengthens and/or the contact angle decreases, then the flow pattern is gradually dominated by irregular interfacial configurations, and the imbibition k_{rnw} increases. The imbibition P_c is a decreasing function of the capillary number or increasing function of the injected phase viscosity in agreement with the linear thermodynamic theory.

* Corresponding author. Tel.: +30 2610 965212; fax: +30 2610 965223.
E-mail address: ctsakir@iceht.forth.gr (C.D. Tsakiroglou).

0301-9322/$ - see front matter © 2005 Elsevier Ltd. All rights reserved.
doi:10.1016/j.ijmultiphaseflow.2005.06.009

Keywords: Capillary pressure; Relative permeability; Immiscible displacement; Capillary number; Pore network; Flow pattern

1. Introduction

Visualization experiments of the unsteady immiscible displacement of two phases in glass-etched pore networks have extensively been used to investigate the pore-scale transport mechanisms, and identify the transient growth patterns as related with a variety of dimensionless parameters such as the capillary number (ratio of viscous to capillary forces), the viscosity ratio (ratio of the viscosity of the injected fluid to the viscosity of displaced fluid), the Bond number (ratio of gravity to capillary forces), and wettability (contact angle) (Lenormand et al., 1988; Birovljev et al., 1991; Vizika et al., 1994; Tzimas et al., 1997). Experimental visualization studies have provided information for the development of dynamic mechanistic simulators of the immiscible displacement in pore networks (Dias and Payatakes, 1986a,b; Lenormand et al., 1988; Aker et al., 1998; Constantinides and Payatakes, 2000; Hughes and Blunt, 2000; Ferer et al., 2003; Singh and Mohanty, 2003). Moreover, diffusion limited aggregation (DLA), invasion percolation and gradient percolation models have also been employed to interpret quantitatively the growth of stabilized and destabilized fronts under the interactions of gravity, capillarity, and viscous forces (Wilkinson, 1986; Gouyet et al., 1988; Cieplak and Robbins, 1990; Ferer et al., 1993, 1995; Zhang and Liu, 1998; Xu et al., 1998).

More recently, the macroscopic two-phase flow equations have been employed to estimate the drainage capillary pressure and relative permeability curves from the transient responses of the axial distribution of the fluid saturation and pressure drop, whereas scaling laws of the gradient percolation theory were used to interpret the variation of estimated parameters with the capillary number (Tsakiroglou et al., 2003a). Moreover, the role of the shear-thinning rheology of the non-wetting phase on the transient evolution of the displacement at the network scale has been clarified for drainage and imbibition experiments (Tsakiroglou et al., 2003b; Tsakiroglou, 2004). In addition, the shift caused on the drainage capillary pressure and relative permeability functions has been interpreted by extending the scaling laws of the gradient percolation theory (Wilkinson, 1986; Xu et al., 1998) and thermodynamic theory of the capillary pressure (Hassanissadeh et al., 2002) to power law fluids (Tsakiroglou, 2004).

The capillary pressure and relative permeability curves of a porous medium are average multiphase transport properties that bridge the gap between the micro-scale flow dynamics and macroscopic flow. Depending on the prevailing flow conditions, the displacement growth pattern may be dominated by a fractal regime (e.g. capillary fingering, viscous fingering, etc.) over the front length scale, which, occasionally, may exceed the sample length (Tsakiroglou et al., 2003b). Evidently, the macroscopic two-phase flow equations are not valid over the fractal frontal region, while the capillary and relative permeability curves vary within this region (Blunt and King, 1991; Singh and Mohanty, 2003; Tsakiroglou et al., 2003a). However, in the practice of core analysis, unsteady-state displacement experiments performed on finite-size cores are employed to estimate the capillary pressure and relative permeability curves (Mejia et al., 1995; Kulkarni et al., 1998; Huang and Honarpour, 1998; Mitlin et al., 1999; Toth et al., 2002). Hence, it would be

interesting to correlate the so-estimated two-phase flow coefficients with all pertinent parameters and evaluate the validity of these coefficients with respect to the pore-scale mechanisms and pore network growth pattern.

In the present study, we extend earlier work (Tsakiroglou et al., 2003a, 2005; Tsakiroglou, 2004) by processing datasets of published (Tsakiroglou et al., 2003b) and unpublished displacement experiments, performed on three different model porous media, by varying the capillary number, wettability, and fluid rheology. Our objective is to complete the investigation of the sensitivity of drainage and imbibition k_{rw}, k_{rnw}, P_c to the abovementioned parameters, and interpret the results in terms of the transient growth pattern identified at the network scale. The capillary pressure and relative permeability curves are estimated from stable and unstable displacements and using Newtonian and shear-thinning non-wetting phases (NWP). Visualization drainage and imbibition experiments are performed on simple and dual pore networks by using three fluid systems: paraffin oil/water coloured with methylene blue, paraffin oil coloured with oil red/water, and shear-thinning dispersion of ozokerite in paraffin oil/aqueous solution of PEG coloured with methylene blue. The measured transient response of the fluid saturation and pressure drop across the pore network are introduced into a numerical scheme of inverse modelling to estimate simultaneously the capillary pressure and relative permeability curves at varying values of the capillary number.

2. Transient experiments of immiscible displacement

Model porous media were fabricated by etching mirror image patterns of simple and dual pore networks (Fig. 1 and Table 1) on two glass plates with hydrofluoric acid, and sintering the pre-aligned etched plates in a programmable furnace (Theodoropoulou et al., 2001; Tsakiroglou et al., 2003a,b). Paraffin oil and distilled water were used as the bases for the formulation of the non-wetting (NWP) and wetting phase (WP), respectively. An intermediate-wet fluid system (contact angle of NWP/WP/glass ~60°) was prepared by colouring the paraffin oil with oil red (Table 2). A water-wet fluid system (contact angle of NWP/WP/glass ~40°) was prepared by colouring the water with methylene blue. Strongly water-wet fluid systems (contact angle of NWP/WP/glass <40°) were prepared by dissolving ozokerite (natural mineral wax) at varying concentrations in paraffin oil to synthesize an inelastic and time-independent shear-thinning NWP (Table 3) and dissolving poly-ethylene-glycol (PEG) in water coloured with methylene blue (Table 2).

Drainage and imbibition experiments (Fig. 2a) were performed on each pore network by displacing the wetting phase (WP) by the non-wetting one (NWP) and vice-versa. For the sake of generality, the symbols I and D, are used to denote the injected and displaced phase, respectively. In drainage experiments, it is I = nw and D = w, while in imbibition experiments, it is I = w and D = nw (Table 2). All experiments were performed at controlled values of the capillary number Ca and viscosity ratio κ, defined by

$$Ca = \mu_I u_I / \gamma_{ow} \quad \text{and} \quad \kappa = \mu_I / \mu_D \tag{1}$$

respectively, where u_I and μ_I are the superficial flow velocity and viscosity of the injected phase, γ_{ow} is the NWP/WP interfacial tension, and μ_D is the viscosity of the displaced fluid. Whenever, the NWP is a shear-thinning fluid, an apparent viscosity, defined in accordance with Darcy's law (Tsakiroglou et al., 2003b), is used in Eq. (1).

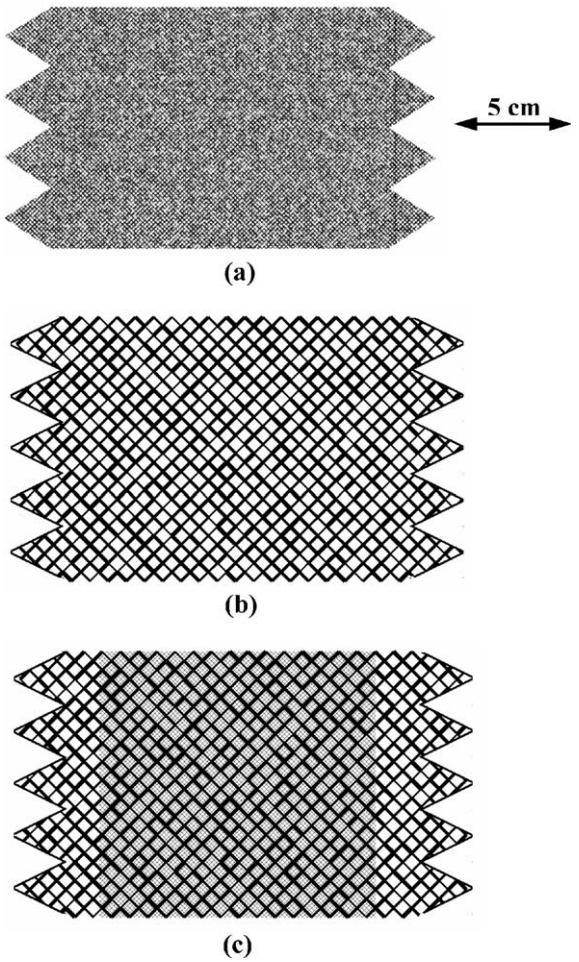

Fig. 1. Patterns of the pore networks used in experiments: (a) model M-1; (b) model S-1; (c) model D-1.

Table 1
Structural properties of pore network models

Property	Model M-1	Model S-1	Model D-1	
			Large pores	Small pores
$\langle w_p \rangle$ (μm)	470	1220	1226	160
σ_w (μm)	168	325	337	6.0
$\langle d_p \rangle$ (μm)	126	172	162	100
σ_d (μm)	20	40	41	20
l_p (μm)	1365	5560	$l_w = 5560$	$l_n = 1390$
$k(D)$	20.26	8.72	7.85 ($l_p = l_w = 5560$ μm)	
			31.4 ($l_p = l_n = 1390$ μm)	

Table 2
Experimental conditions and physicochemical properties of fluid systems

Displaced phase (D)	Injected phase (I)	θ_e (°)	Ca	γ_{ow} (N/m)	μ_w (Pa s)	μ_{nw} (Pa s)	Ca_P	Ca_N	Model
Paraffin oil coloured with oil red (nw)	Distilled water (w)	60	10^{-5}	32×10^{-3}	0.001	0.026	1.6	80.3	M-1
Paraffin oil coloured with oil red (nw)	Distilled water (w)	60	10^{-6}	32×10^{-3}	0.001	0.026	0.16	8.03	M-1
Paraffin oil coloured with oil red (nw)	Distilled water (w)	60	10^{-7}	32×10^{-3}	0.001	0.026	0.016	0.80	M-1
Distilled water (w)	Paraffin oil coloured with oil red (nw)	60	0.8×10^{-6}	32×10^{-3}	0.001	0.026	0.066	0.81	S-1
Paraffin oil coloured with oil red (nw)	Distilled water (w)	60	1.1×10^{-6}	32×10^{-3}	0.001	0.026	2.38	29.2	S-1
Paraffin oil coloured with oil red (nw)	Distilled water (w)	60	1.1×10^{-8}	32×10^{-3}	0.001	0.026	0.024	0.29	S-1
Dispersion of ozokerite ($x_{OZ}=0.02$) in paraffin oil (nw)	Aqueous solution of PEG ($x_{PEG}=0.08$) coloured with methylene blue (w)	32	0.8×10^{-6}	24×10^{-3}	0.0019	0.05	1.024	12.5	S-1
Dispersion of ozokerite ($x_{OZ}=0.02$) in paraffin oil (nw)	Aqueous solution of PEG ($x_{PEG}=0.33$) coloured with methylene blue (w)	8	0.5×10^{-6}	20×10^{-3}	0.0439	1.141	0.55	6.67	S-1
Distilled water (w)	Paraffin oil coloured with oil red (nw)	60	0.8×10^{-6}	32×10^{-3}	0.001	0.026	0.069[a] 0.023[b]	0.85 0.09	D-1
Paraffin oil coloured with oil red (nw)	Distilled water (w)	60	0.8×10^{-6}	32×10^{-3}	0.001	0.026	2.0 0.15	24.5 0.6	D-1
Paraffin oil coloured with oil red (nw)	Distilled water (w)	60	1.1×10^{-8}	32×10^{-3}	0.001	0.026	0.027 0.002	0.33 0.008	D-1
Paraffin oil (nw)	Distilled water coloured with methylene blue	41	0.8×10^{-6}	32×10^{-3}	0.001	0.026	1.33 0.4	16.2 1.6	D-1
Paraffin oil (nw)	Distilled water coloured with methylene blue	41	10^{-7}	32×10^{-3}	0.001	0.026	0.16 0.05	2.03 0.2	D-1
Dispersion of ozokerite ($x_{OZ}=0.02$) in paraffin oil (nw)	PEG solution ($x_{PEG}=0.055$) coloured with methylene blue (w)	38	0.8×10^{-6}	20×10^{-3}	0.0025	0.065	1.27 0.38	15.5 1.53	D-1

[a] network of large pores.
[b] sub-network of small pores.

Table 3
Rheological parameters of mixed Meter-and-power law fluid model $\mu_{nw} = \mu_c^{1/m}\sigma^{1-1/m} + \frac{\mu_0 - \mu_c^{1/m}\sigma^{1-1/m}}{1+(\sigma/\sigma_c)^{n-1}}\mu(\sigma_s) = \mu_s$

Ozokerite concentration in synthetic NWP	$x_{OZ} = 0.02$
μ_0 (Pa s)	0.886
μ_c (Pa s)	0.105
σ_c (Pa)	0.118
n	4.3
m	0.82
μ_s (Pa s)	0.026
σ_s (Pa)	60.6

At each experiment, the transient response of the total NWP or WP saturation, and occasionally, of its axial distribution across the pore network, was measured with image analysis, and the transient response of the pressure difference across the viewed region of the pore network was measured with a differential pressure transducer (Tsakiroglou et al., 2003b). The viewed area of the pore network is located far from the inlet and outlet ends (Fig. 2b), so that any boundary effects on the experimental results are minimized, and the pore system (Fig. 2a) can be regarded as a piece of a semi-infinite homogeneous porous medium. This simplifying assumption enables us to solve the two-phase flow equations in a very long porous medium and then calculate all experimentally measured variables (Tsakiroglou et al., 2003a,b, 2005; Tsakiroglou, 2004).

3. Two-phase flow equations and parameter estimation

In a homogeneous and isotropic porous medium of permeability k and porosity ε, the one-dimensional immiscible displacement of a Newtonian wetting fluid (w) by a non-Newtonian non-wetting one (nw) and vice-versa, is described by the following averaged mass and momentum balances (Bear, 1972; Sahimi, 1995; Tsakiroglou, 2004):

$$\varepsilon\frac{\partial S_{nw}}{\partial t} + \frac{\partial u_{nw}}{\partial x} = 0, \tag{2}$$

$$\varepsilon\frac{\partial S_{w}}{\partial t} + \frac{\partial u_{w}}{\partial x} = 0, \tag{3}$$

$$u_w = \frac{kk_{rw}}{\mu_w}\left(-\frac{\partial P_w}{\partial x}\right), \tag{4}$$

$$u_{nw} = \frac{k'k_{rnw}}{\langle\mu_{nw}\rangle}\left(-\frac{\partial P_{nw}}{\partial x}\right), \tag{5}$$

where S_j, P_j, u_j, k_{rj}, μ_j ($j = w, nw$) are the saturation, pressure, superficial velocity, relative permeability, and viscosity of the phase j. For a shear-thinning NWP, the effective permeability, k', and average viscosity, $\langle\mu_{nw}\rangle$, are nonlinear functions of the pressure gradient $-\partial P_{nw}/\partial x$, fluid rheology and pore structure (Tsakiroglou, 2002). In a dual pore network these properties are calculated from the corresponding ones of the component sub-networks (Appendix A). The capillary pressure is defined as the difference between the local pressures of the two fluids and is written as

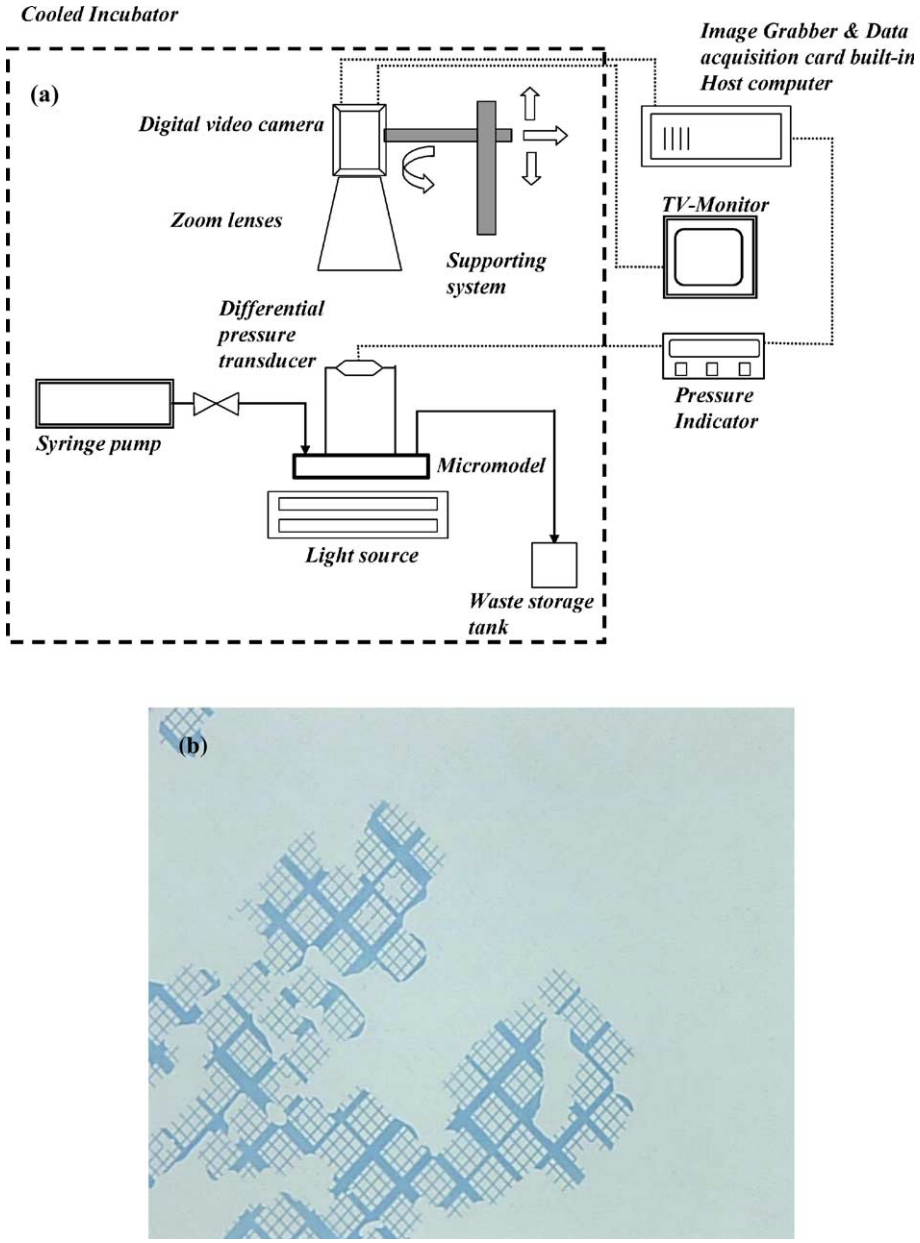

Fig. 2. (a) Experimental setup. (b) Snap-shot of the displacement of NWP (paraffin oil–white fluid) by WP (distilled water coloured with methylene blue–dark fluid).

$$P_c = P_{nw} - P_w, \tag{6}$$

whereas the fluid saturations are interrelated by

$$S_w + S_{nw} = 1.0. \tag{7}$$

By substituting the fluid flow velocity, u_{nw}, with the fractional flow, F_{nw}, defined by

$$F_{nw} = \frac{u_{nw}}{u_0}, \quad 0 \leqslant F_{nw} \leqslant 1.0 \tag{8}$$

and using the dimensionless variables

$$\xi = \frac{x}{L} \quad \text{and} \quad \tau = \frac{u_0 t}{\varepsilon L}. \tag{9}$$

Eqs. (2)–(7) are transformed to

$$\frac{\partial S_{nw}}{\partial \tau} + \frac{\partial F_{nw}}{\partial \xi} = 0, \tag{10}$$

$$F_{nw} = \frac{g k_{rnw}}{g k_{rnw} + k_{rw}} \left[1 - \frac{u_c}{u_0} k_{rw} \frac{\partial P_c^*}{\partial \xi}\right], \tag{11}$$

$$\left(-\frac{\partial P_{nw}^*}{\partial \xi}\right) = \left(\frac{u_0}{u_c}\right) \frac{1}{g k_{rnw} + k_{rw}} \left[1 - \frac{u_c}{u_0} k_{rw} \frac{\partial P_c^*}{\partial \xi}\right], \tag{12}$$

where g is a nonlinear function of the pressure gradient, $-\partial P_{nw}/\partial x$, given by

$$g = \frac{k'}{\langle \mu_{nw} \rangle} \frac{\mu_w}{k}, \tag{13}$$

the dimensionless variables P_c^* and P_{nw}^* are defined by

$$P_c^* = \frac{P_c}{\Delta P_t^0}, \quad P_{nw}^* = \frac{P_{nw}}{\Delta P_t^0}, \tag{14}$$

whereas the characteristic velocity u_c is defined by

$$u_c = \frac{k \Delta P_t^0}{\mu_w L} \tag{15}$$

and ΔP_t^0 is the experimentally measured steady-state total pressure drop across the pore network. Considering that, the local capillary pressure and relative permeabilities depend solely on S_{nw}, and employing, Eqs. (10)–(12), we finally get a system of coupled and nonlinear PDEs with independent variables ξ, τ and dependent variables S_{nw} and $(-\partial P_{nw}^*/\partial \xi)$ (Tsakiroglou, 2004).

The capillary pressure and relative permeability curves are represented by the following Corey type functions:

(a) Primary drainage processes where the NWP displaces the WP and the irreducible WP saturation is $S_{wi} (0 \leqslant S_{nw} \leqslant 1 - S_{wi})$

$$P_c = P_c^0 \left(1 - \frac{S_{nw}}{1 - S_{wi}} + b_c\right)^{-m_c}, \tag{16}$$

$$k_{rw} = k_{rw}^0 \left(1 - \frac{S_{nw}}{1 - S_{wi}} + b_w\right)^{m_w} \left(\frac{1}{1 + b_w}\right)^{m_w}, \tag{17}$$

$$k_{rnw} = k_{rnw}^0 \left(\frac{S_{nw}}{1 - S_{wi}} + b_{nw}\right)^{m_{nw}} \left(\frac{1}{1 + b_{nw}}\right)^{m_{nw}}. \tag{18}$$

(b) Primary imbibition processes where the WP displaces the NWP and the residual NWP saturation is $S_{nwr}(0 \leqslant S_w \leqslant 1 - S_{nwr})$

$$P_c = P_c^0\left(\frac{S_w}{1 - S_{nwr}} + b_c\right)^{-m_c}, \tag{19}$$

$$k_{rw} = k_{rw}^0\left(\frac{S_w}{1 - S_{nwr}} + b_w\right)^{m_w}\left(\frac{1}{1 + b_w}\right)^{m_w}, \tag{20}$$

$$k_{rnw} = k_{rnw}^0\left(1 - \frac{S_w}{1 - S_{nwr}} + b_{nw}\right)^{m_{nw}}\left(\frac{1}{1 + b_{nw}}\right)^{m_{nw}}. \tag{21}$$

The parameters P_c^0, m_c, m_w, m_{nw} can be considered as nonlinear functions of Ca and κ. The end relative permeability k_D^0 is equal to unity, whereas the end relative permeability, k_I^0, is computed numerically from Eq. (4) or (5), by setting $u_I = u_0$ and assuming that $(-\partial P_I/\partial x) = \Delta P_t^0/L$.

Modal values and confidence intervals of P_c^0, m_c, m_w, m_{nw} were so estimated that the numerically calculated transient responses of $S_{It}(\tau)$ and $\Delta P_t^*(\tau)$ match the corresponding experimental datasets (history matching). The parameter estimation was carried out by using the ATHENA visual workbench software (Tsakiroglou et al., 2003a, 2005; Tsakiroglou, 2004). The values of b_c, b_w, b_{nw} were kept constant and equal to very small numbers (10^{-4}–10^{-3}).

4. Displacement growth patterns and two-phase flow coefficients

4.1. Imbibition experiments in model M-1

Two scale-dependent capillary numbers Ca_P and Ca_N are defined by

$$Ca_p = \beta Ca\frac{\langle r_H\rangle l_p}{k\cos\theta_e} \tag{22a}$$

and

$$Ca_p = \beta Ca\frac{\langle r_H\rangle L_N}{k\cos\theta_e} \tag{22b}$$

respectively, where l_p is the pore length, L_N the network length, and $\langle r_H\rangle$ is an average hydraulic pore radius (Tsakiroglou, 2002). Ca_p and Ca_N are used to estimate roughly the ratio of viscous to capillary forces at the pore- and network-scale, respectively. Given that $\mu_{nw} \gg \mu_w$, the coefficient $\beta = 1/\kappa$ for imbibition (Tsakiroglou et al., 2003b) and $\beta = 1$ for drainage (Tsakiroglou et al., 2003a).

Under an unfavourable viscosity ratio ($\kappa \ll 1$) and intermediate wettability ($\theta_e = 60°$) the displacement growth pattern is dominated by viscous fingers, capillary fingers, or a mixture of both at high (Fig. 3a), low (Fig. 3c) or intermediate (Fig. 3b) Ca values, respectively (Table 2). The discrepancy between the experimentally measured and numerically computed responses of $S_{wt}(\tau)$ and $\Delta P_t^*(\tau)$ at high Ca values (Fig. 4a and b) is associated with the ramified and fractal structure of the viscous fingering pattern (Tsakiroglou et al., 2005) and its deviation from the compact one-dimensional displacement of the macroscopic approach (Fig. 3a). At intermediate and low Ca values,

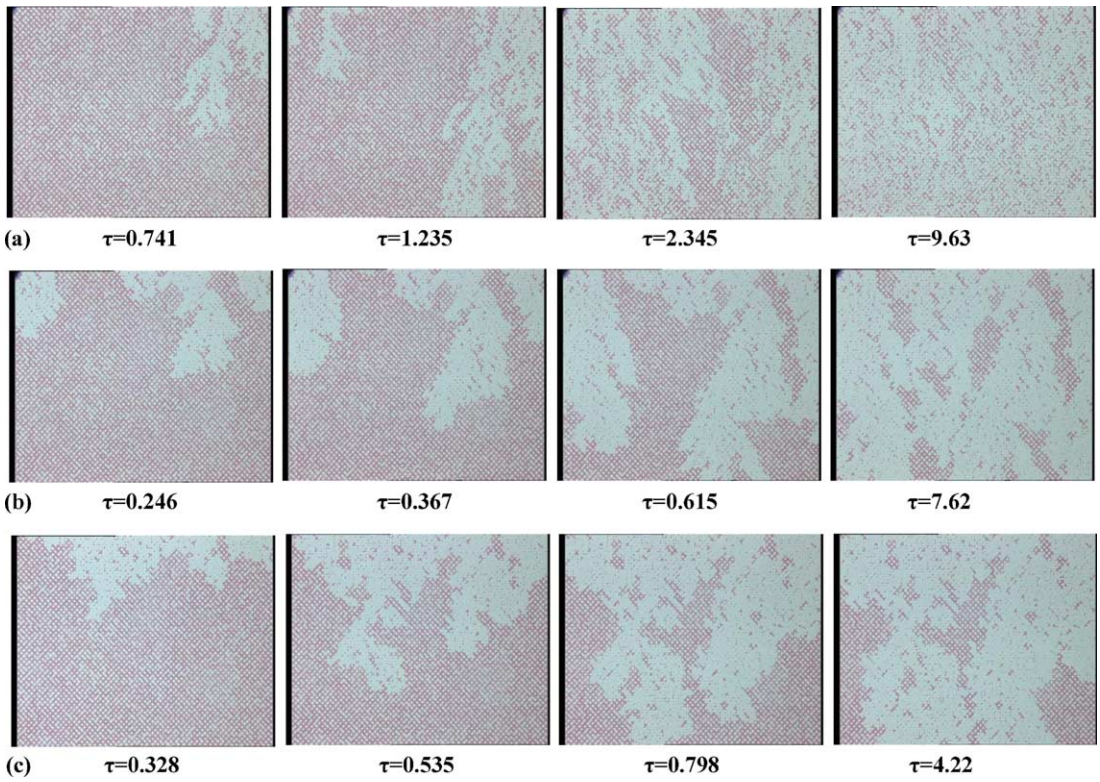

Fig. 3. Imbibition growth pattern in model M-1 where paraffin oil coloured with oil red (Newtonian NWP) is displaced by distilled water at (a) $Ca = 10^{-5}$, (b) $Ca = 10^{-6}$, (c) $Ca = 10^{-7}$.

the fingers become more compact, the two-phase flow pattern tends to the linear one (Fig. 3b and c), and the experimental responses of $S_{wt}(\tau)$ and $\Delta P_t^*(\tau)$ fit satisfactorily to the numerical predictions of the inverse modelling scheme (Fig. 4c–f). In general, the estimated k_{rw} is an increasing function of Ca, while the k_{rnw} is a decreasing function of Ca (Fig. 5, Table 4). At high Ca values (Fig. 3a), the tip-splitting and lateral growth of viscous fingers lead to the fast creation of network spanning pathways of the WP and the destruction of the continuity of the NWP (Fig. 3a). This, in turn, is reflected in the sharp increase of k_{rw} and decrease of k_{rnw} at high Ca values (Fig. 5). An analogous behaviour was also confirmed in imbibition experiments performed on the same model porous medium M-1 (Tsakiroglou et al., 2005) by using a water-wet fluid system ($\theta_e = 40°$).

The strong sensitivity of the non-equilibrium P_c to Ca (Table 4) can be envisaged in the light of the macroscopic theory of the capillary pressure (Hassanissadeh et al., 2002). This is expressed by the relationship (Tsakiroglou et al., 2003a; Tsakiroglou, 2004)

$$-\left(\frac{Ca_{\gamma ow}}{L\mu_I}\right)\lambda_m \frac{\partial S_{wt}}{\partial \tau} = P_c - P_{c,stat}, \tag{23}$$

where λ_m is a material coefficient, the factor $Ca\lambda_m$ is almost constant (Tsakiroglou et al., 2003a), $P_{c,stat}$ is defined thermodynamically to be equal to the change in the free energy of the system as a

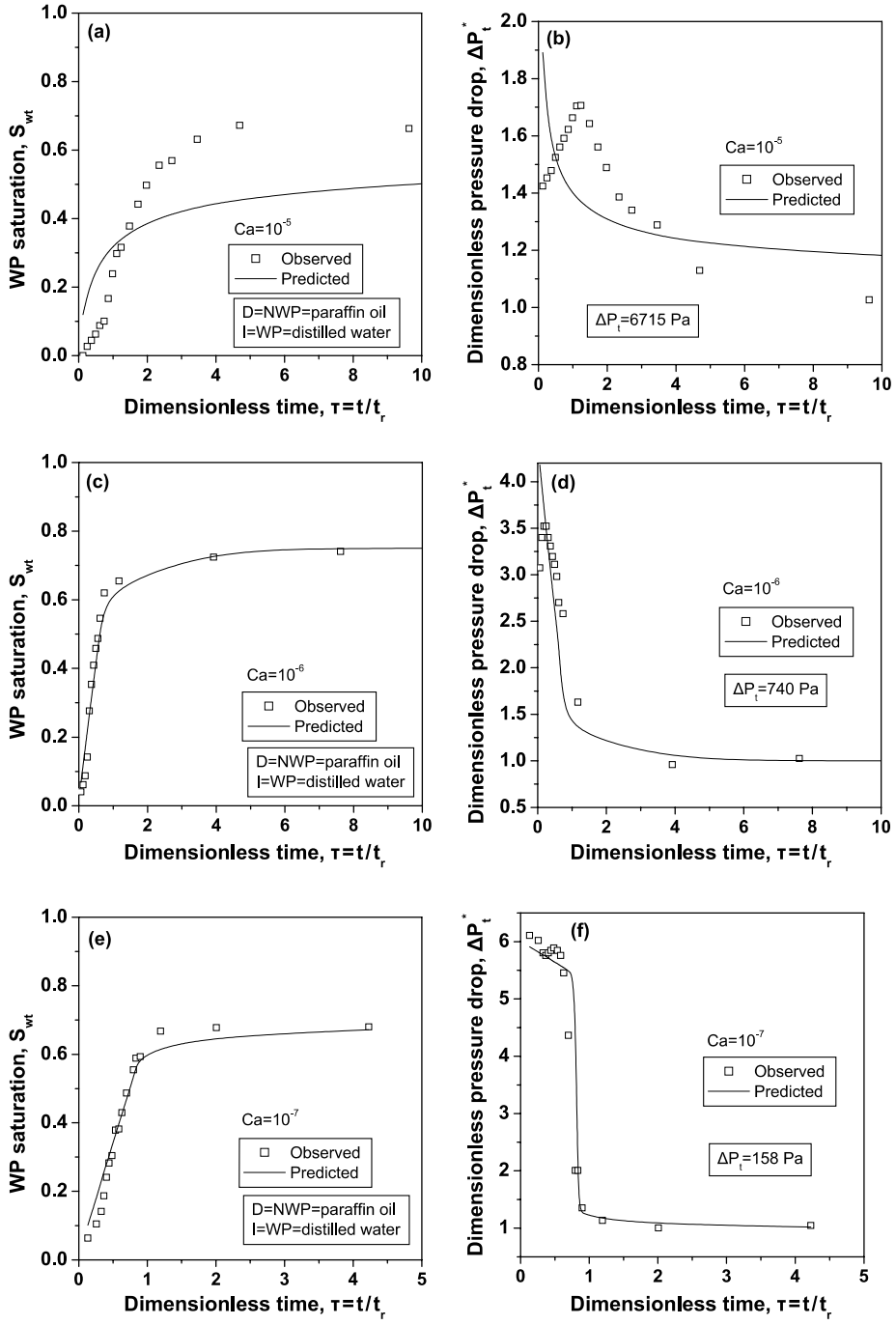

Fig. 4. Comparison of experimentally measured (Fig. 3) with numerically predicted (a) (c) (e) total NWP saturation, and (b) (d) (f) dimensionless total pressure drop, at (a, b) $Ca = 10^{-5}$, (c, d) $Ca = 10^{-6}$, (e, f) $Ca = 10^{-7}$. The parameter values of Table 4 are used.

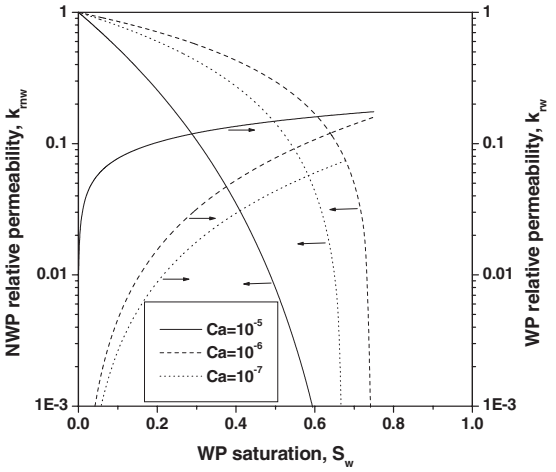

Fig. 5. Imbibition relative permeability curves of model porous medium M-1 estimated from displacement experiments at three Ca values (Fig. 3).

Table 4
Parameters of k_{rw}, k_{rnw}, P_c estimated from displacement experiments performed on model M-1

Displacement	NWP	WP	Ca	P_c^0 (Pa)	m_c (b_c)	k_{rw}^0	m_w (b_w)	k_{rnw}^0	m_{nw} (b_{nw})
Imbibition	Paraffin oil with oil red	Distilled water	10^{-5}	40.0	10^{-4} (10^{-4})	0.175	0.407 ± 0.0954 (10^{-4})	1.0	4.4 ± 1.77 (10^{-4})
Imbibition	Paraffin oil with oil red	Distilled water	10^{-6}	236.6 ± 222.7	1.7×10^{-6} (10^{-4})	0.159	1.76 ± 0.057 (10^{-4})	1.0	1.105 ± 0.35 (10^{-4})
Imbibition	Paraffin oil with oil red	Distilled water	10^{-7}	642.3 ± 33.1	7.8×10^{-10} (10^{-4})	0.075	1.745 (10^{-4})	1.0	1.463 (10^{-4})

result of a change in the wetting phase saturation, whereas the viscosity of the injected phase, μ_I may also change with Ca for a shear-thinning NWP (Table 2). The entry capillary pressure P_c^0 is a decreasing function of Ca (Table 4), and such a behaviour agrees completely with the linear theory of the dynamic capillary pressure, Eq. (23), for transient imbibition processes where $\partial S_{wt}/\partial \tau > 0$.

4.2. Drainage and imbibition experiments in model S-1

In model S-1, the measured network area consists of a relatively small number of pores and unavoidably the transient growth pattern (Fig. 6a) may differ substantially from that observed during a displacement in a large pore network. In drainage experiments under favourable viscosity ratio ($\kappa \gg 1$), the thickness of the frontal region, dominated by the capillary forces (Tsakiroglou et al., 2003a), becomes comparable to the length of the measured area (Fig. 6a) so that capillary fingering is the dominant pattern at the network scale (Table 2), and unavoidably a discrepancy between measured and predicted responses of $S_{nwt}(\tau)$ and $\triangle P_t^*(\tau)$ is expected (Fig. 7a and b).

Under an unfavourable viscosity ratio ($\kappa \ll 1$), the imbibition growth pattern in S-1 consists of segments of viscous (Fig. 6b) or capillary (Fig. 6c) fingers, the lateral growth of which is enhanced

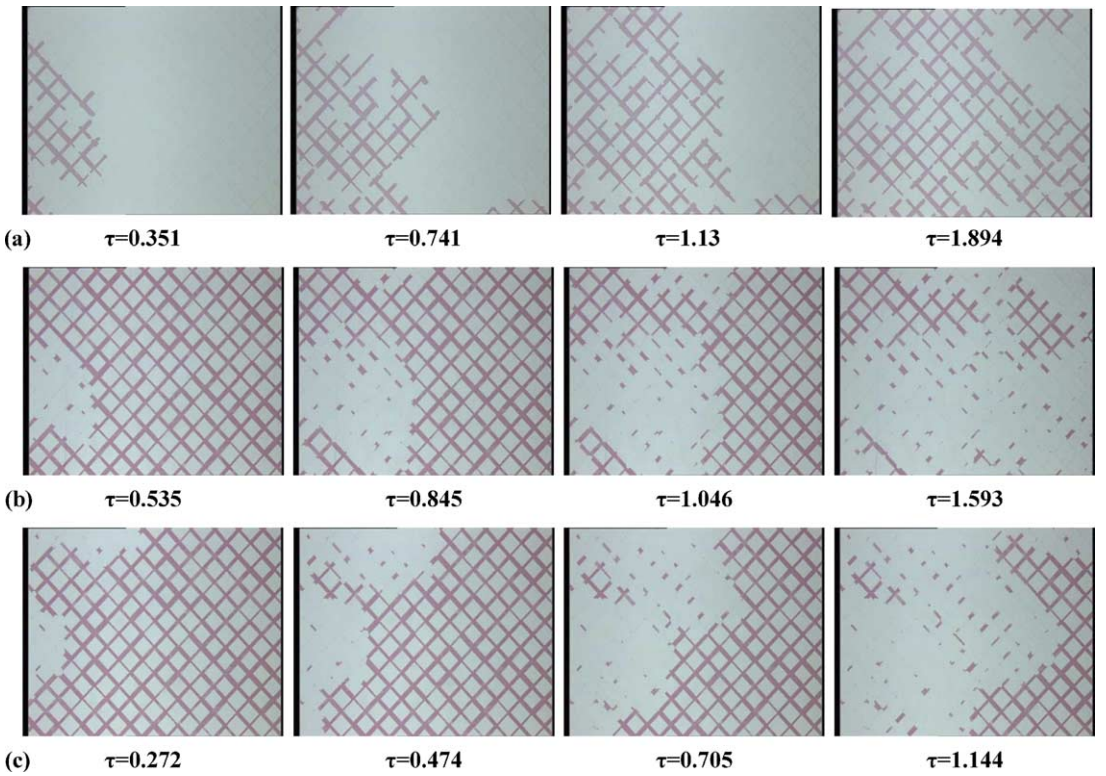

Fig. 6. (a) Drainage growth pattern in model S-1 where distilled water (white) is displaced by paraffin oil coloured with oil red (dark) at $Ca = 0.8 \times 10^{-6}$. (b) Imbibition growth pattern in model S-1 where paraffin oil coloured with oil red (Newtonian NWP) is displaced by distilled water at $Ca = 1.1 \times 10^{-6}$. (c) Imbibition growth pattern in model S-1 where paraffin oil coloured with oil red (Newtonian NWP) is displaced by distilled water at $Ca = 1.1 \times 10^{-8}$.

as the *Ca* decreases. In the first case (Fig. 6b), the viscous forces are the dominant ones over the pore and network scales (Table 2), while in the second case (Fig. 6c), the capillary forces are the dominant ones over both scales (Table 2). The discrepancy observed between measured and predicted responses of $S_{wt}(\tau)$ and $\triangle P_t^*(\tau)$ is pronounced at high *Ca* values (Fig. 7c and d) where the growth of the elongated viscous fingers deviates from the assumption of the 1-D compact displacement (Fig. 6b). The numerical prediction of experimental datasets is improved at low *Ca* values (Fig. 7e and f) where the displacement advances in a more compact fashion (Fig. 6c) because of the cluster-growth mechanism which is explained in detail below. The hysteresis observed between the drainage and imbibition relative permeability curves (Fig. 8) arises from the different flow paths followed by the two fluids during the corresponding displacements (Fig. 6a and b). In contrast to the relative permeabilities of model M-1 (Fig. 5), the imbibition k_{rnw} and k_{rw} are clearly increasing functions of *Ca* (Fig. 8) because the length of the pore network is so small that the tip-splitting of viscous fingers does not influence the hydraulic continuity of the NWP (Fig. 6b). The entry capillary pressure of imbibition, P_c^0, is a decreasing function of *Ca* (Table 5) in agreement with the thermodynamic theory of the capillary pressure, Eq. (23).

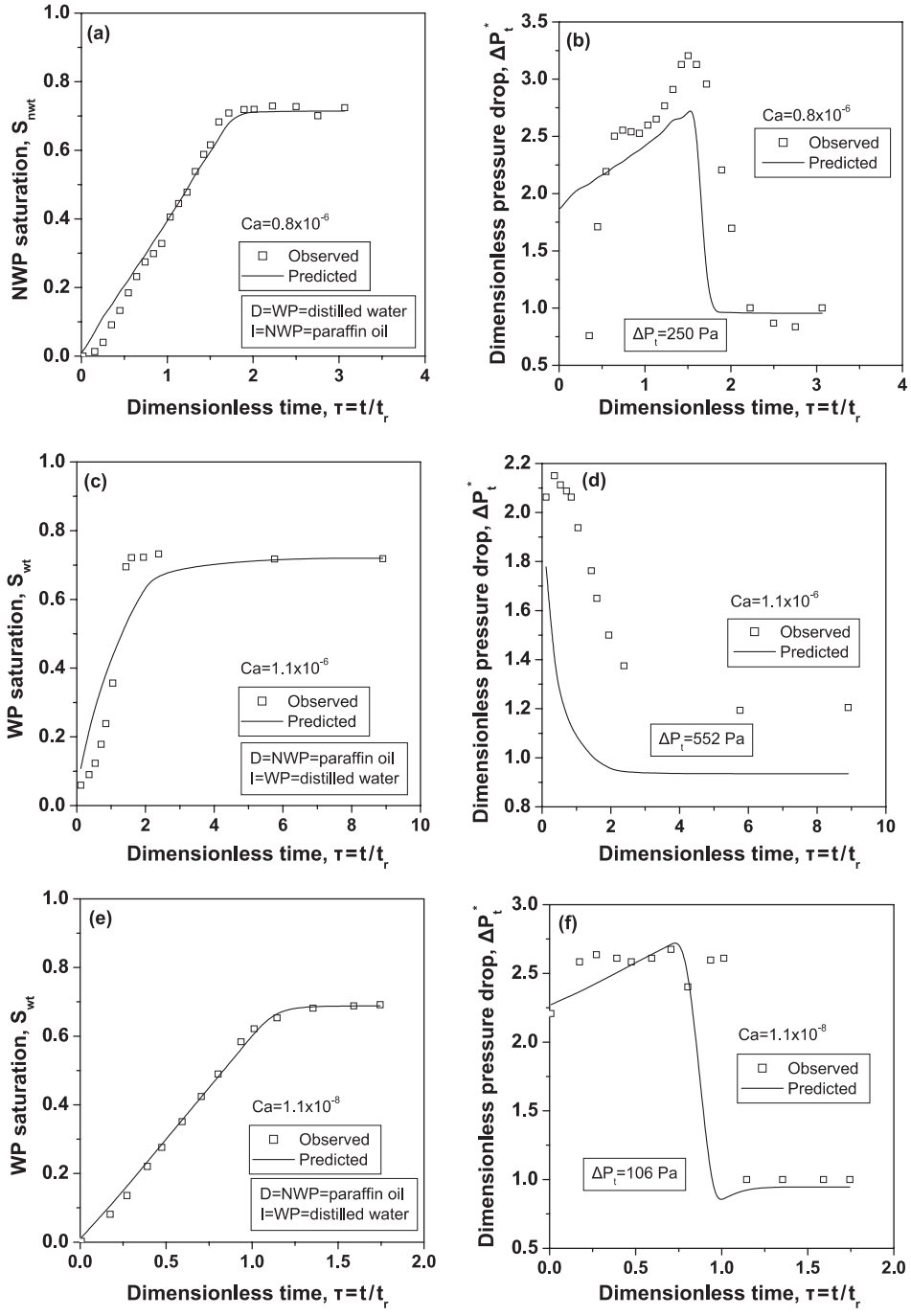

Fig. 7. Comparison of experimentally measured (Fig. 6) with numerically predicted (a) (c) (e) total NWP saturation, and (b) (d) (f) dimensionless total pressure drop, for (a, b) drainage and $Ca = 0.8 \times 10^{-6}$, (c, d) imbibition and $Ca = 1.1 \times 10^{-6}$, (e, f) imbibition and $Ca = 1.1 \times 10^{-8}$. The parameter values of Table 5 are used.

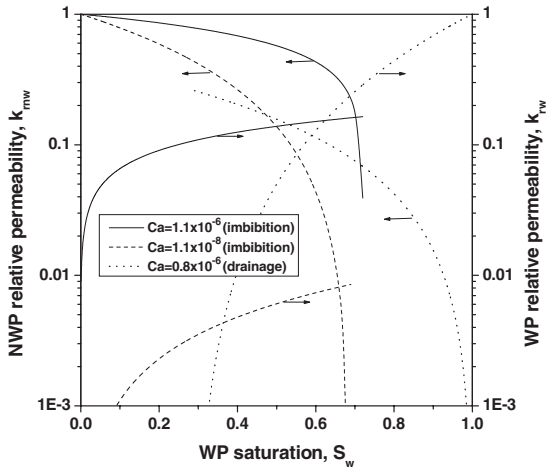

Fig. 8. Drainage and imbibition relative permeability curves of model porous medium S-1 estimated from displacement experiments at three *Ca* values (Fig. 6).

The displacement of a shear-thinning NWP by a Newtonian WP is dominated by viscous forces (Fig. 9, Table 2). At high values of the pore width-to-depth aspect ratio, the precursor advancement-swelling mechanism, which is described in detail elsewhere (Tsakiroglou et al., 2003b, 2005), is evident under water-wet conditions (Fig. 9a) and becomes the dominant flow mechanism under strongly water-wet conditions (Fig. 9b). This mechanism results in the creation of irregular interfacial configurations over the pore network (Fig. 9b), and originates from the advancement of WP precursor films along pore edges, as the piston-type motion of a meniscus is not favoured by the local fluid topology (e.g. pore junctions) and local pressure field (e.g. a high pressure drop is required for the frontal displacement of the high viscosity NWP). The macroscopic two-phase

Table 5
Parameters of k_{rw}, k_{rnw}, P_c estimated from displacement experiments performed on model S-1

Displacement	NWP	WP	*Ca*	P_c^0 (Pa)	m_c (b_c)	k_{rw}^0	m_w (b_w)	k_{rnw}^0	m_{nw} (b_{nw})
Drainage	Paraffin oil with oil red	Distilled water	0.8 $\times 10^{-6}$	460.8 $\pm$ 109.6	0.0296 $\pm$ 0.0083 (10^{-4})	1.0	2.535 $\pm$ 0.69 (10^{-4})	0.266	1.437 $\pm$ 0.00024 (10^{-4})
Imbibition	Paraffin oil with oil red	Distilled water	1.1 $\times 10^{-6}$	-5.77	0.00137 (10^{-3})	0.164	0.465 $\pm$ 0.202 (10^{-3})	1.0	0.469 (10^{-3})
Imbibition	Paraffin oil with oil red	Distilled water	1.1 $\times 10^{-8}$	217.8 $\pm$ 47.1	1.0×10^{-6} (10^{-4})	0.0085	1.059 $\pm$ 0.16 (10^{-4})	1.0	1.535 $\pm$ 0.754 (10^{-4})
Imbibition	Ozokerite in paraffin oil	Aqueous PEG solution	0.8 $\times 10^{-6}$	1.2×10^{-4}	1.0×10^{-5} (10^{-3})	0.0616	1.239 (10^{-4})	1.0	0.9908 (10^{-4})
Imbibition	Ozokerite in paraffin oil	Aqueous PEG solution	0.5 $\times 10^{-6}$	24.01 $\pm$ 36.4	8.1×10^{-6} (10^{-3})	0.111	1.567 $\pm$ 0.0267 (10^{-4})	1.0	0.502 $\pm$ 0.0016 (10^{-4})

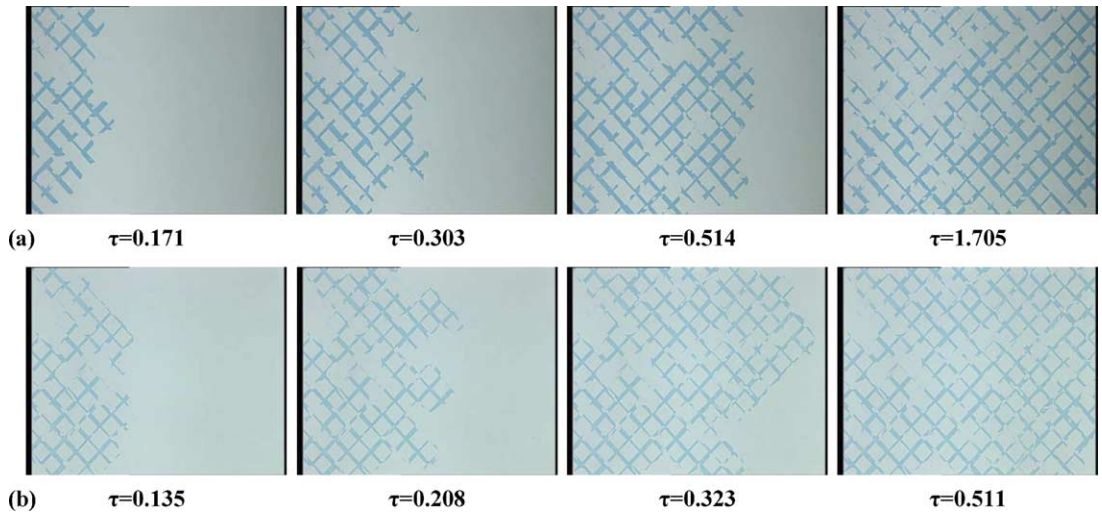

Fig. 9. (a) Imbibition growth pattern in model S-1 where a dispersion of ozokerite ($x_{OZ} = 0.02$) in paraffin oil (shear-thinning NWP) is displaced by an aqueous solution of PEG ($x_{PEG} = 0.08$) coloured with methylene blue (dark) at $Ca = 0.8 \times 10^{-6}$. (b) Imbibition growth pattern in model S-1 where a dispersion of ozokerite ($x_{OZ} = 0.02$) in paraffin oil (shear-thinning NWP) is displaced by an aqueous solution of PEG ($x_{PEG} = 0.33$) at $Ca = 0.5 \times 10^{-6}$.

flow equations are based on the assumption that each fluid flows across its own pathway (Whitaker, 1986). However, this assumption fails under mildly or strongly water-wet conditions favouring the coexistence of both fluids across individual pores (Fig. 9a and b). Therefore, the discrepancy observed between experiment and numerical simulation with respect to $\triangle P_t^*(\tau)$ is reasonable (Fig. 10b and d). Regardless of the prevailing mechanism, the predictability of the transient response of the $S_{wt}(\tau)$ is satisfactory (Fig. 10a and c). As θ_e decreases, the precursor advancement-swelling mechanism enhances the mobility of WP through films flowing along pore edges, and favours the preservation of the continuity of the NWP. In other words both the k_{rnw} and k_{rw} increase with θ_e decreasing (Fig. 11).

4.3. Drainage and imbibition experiments in model D-1

In drainage experiments, the NWP invades the large pores of the dual pore network D-1, while the WP becomes trapped primarily in the sub-networks of the small pores which are bypassed by the NWP (Fig. 12a). Because of the relatively small dimensions of the pore network, the two-phase flow pattern is governed by the capillary fingering mechanism prevailing in the frontal region of a macroscopic displacement (Figs. 6a and 12a).

In imbibition experiments under intermediate-wet conditions, the NWP is trapped in the sub-networks of small pores (Fig. 12b and c). With reference to Ca_p and Ca_N the transient flow pattern is dominated by viscous forces at high Ca values (Fig. 12b and Table 2) and capillary forces at low Ca values (Fig. 12c and Table 2). The two viscous fingers observed at high Ca values (Fig. 12b) are due to the small width of the porous medium compared to the width of the finger. The compact growth pattern observed at low Ca values (Fig. 12c) arises from differences in the

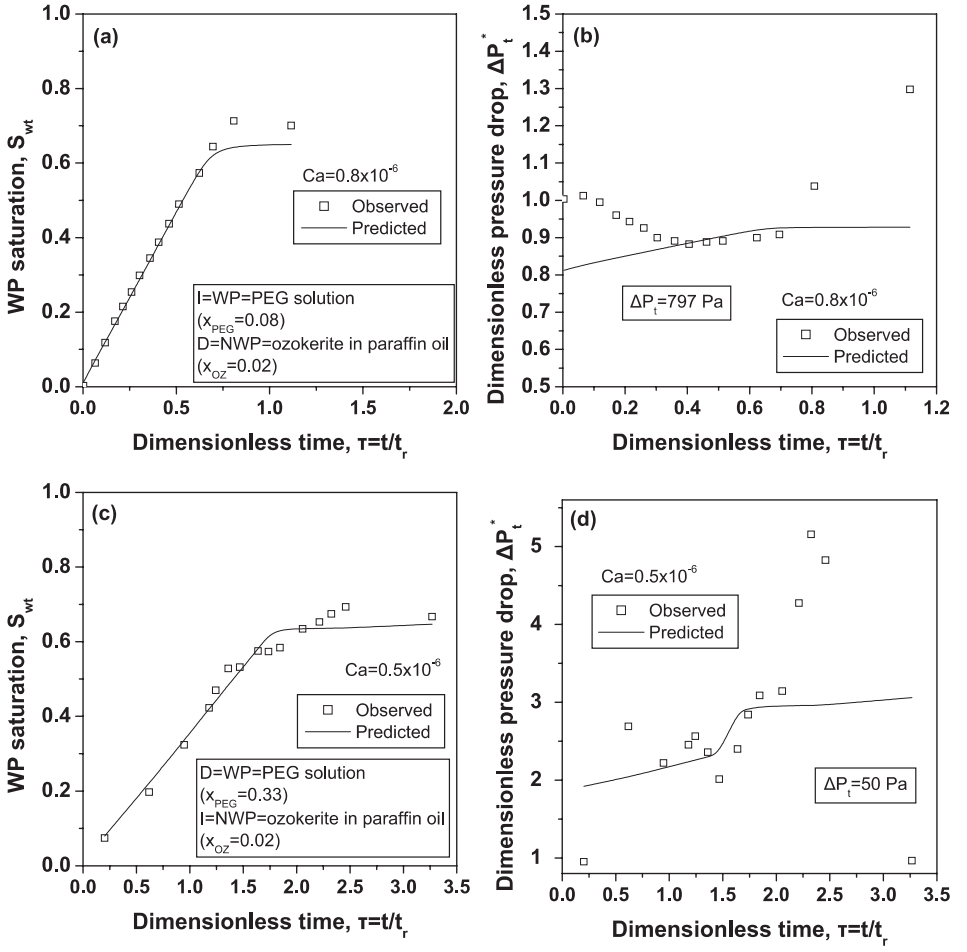

Fig. 10. Comparison of experimentally measured (Fig. 9) with numerically predicted (a) (c) total NWP saturation, and (b) (d) dimensionless total pressure drop, for (a, b) $Ca = 0.8 \times 10^{-6}$, (c, d) $Ca = 0.5 \times 10^{-6}$. The parameter values of Table 5 are used.

critical capillary pressures of the various pore-scale flow events that may occur at the pore junctions (Tsakiroglou and Payatakes, 1998). Under quasi-static conditions, and relatively high values of the contact angle (Table 2), the pore scale mechanisms of menisci motion are not affected only by the dimensions of the individual pores but also by the local fluid topology (Tsakiroglou and Payatakes, 1998). In this manner, certain types of pore emptying or fluid disconnection events, normally occurring at high capillary pressures, are "shadowed" by the prevailing interfacial configurations, and occur spontaneously at lower capillary pressures. The simultaneous occurrence of such non-equilibrium events leads locally to the cluster growth mechanism, and results in a compact flow pattern (Fig. 12c).

The deviation of the drainage flow pattern (Fig. 12a) from the linear displacement is reflected in the discrepancy of the simulated from the experimental responses of $S_{\mathrm{nwt}}(\tau)$ and $\Delta P_{\mathrm{t}}^{*}(\tau)$ (Fig. 13a

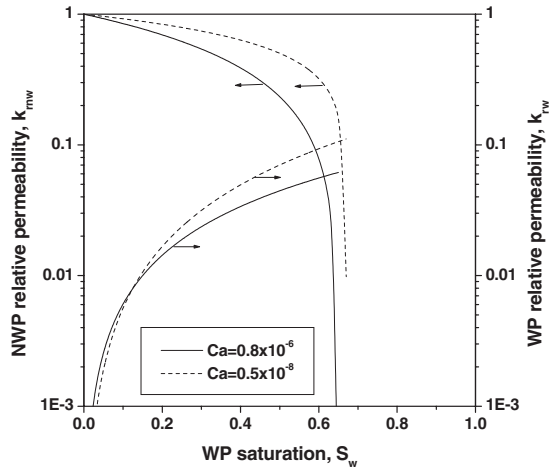

Fig. 11. Imbibition relative permeability curves of model porous medium S-1 estimated from displacement experiments of shear-thinning NWP at two Ca and θ_e values (Fig. 9).

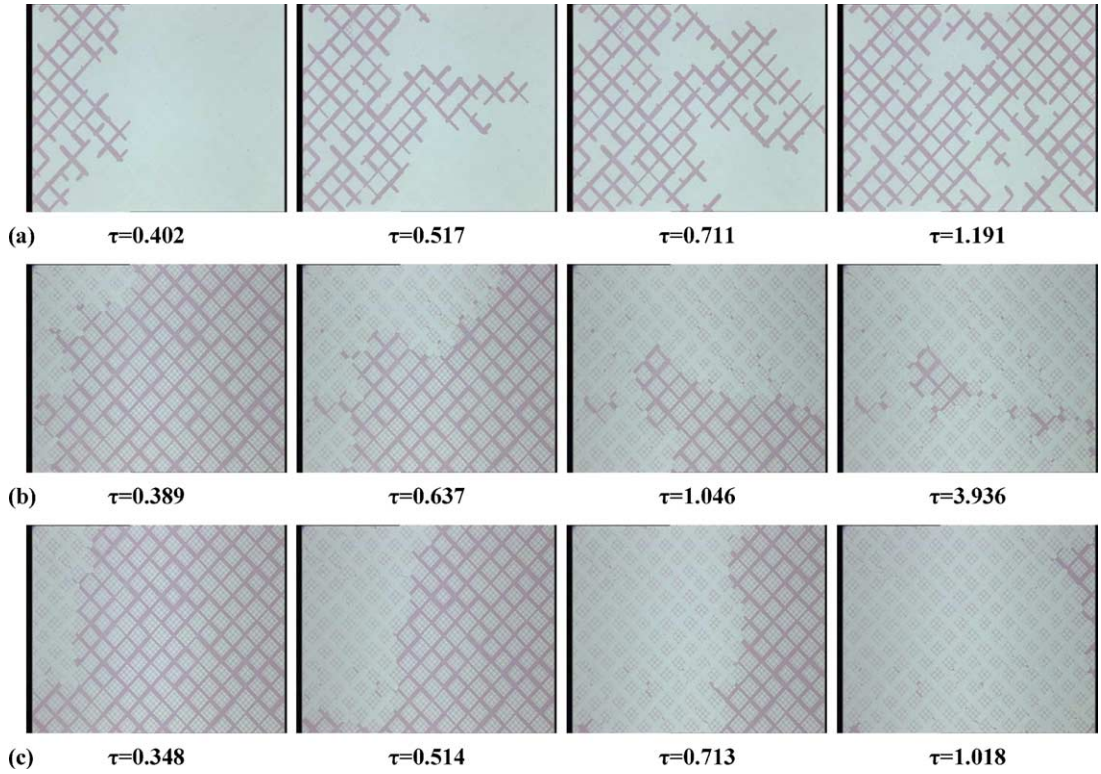

Fig. 12. (a) Drainage growth pattern in model D-1 where distilled water is displaced by paraffin oil coloured with oil red (Newtonian NWP) at $Ca = 0.8 \times 10^{-6}$. (b) Imbibition growth pattern in model D-1 where paraffin oil coloured with oil red (Newtonian NWP) is displaced by distilled water at $Ca = 0.8 \times 10^{-6}$. (c) Imbibition growth pattern in model D-1 where paraffin oil coloured with oil red (Newtonian NWP) is displaced by distilled water at $Ca = 1.1 \times 10^{-8}$.

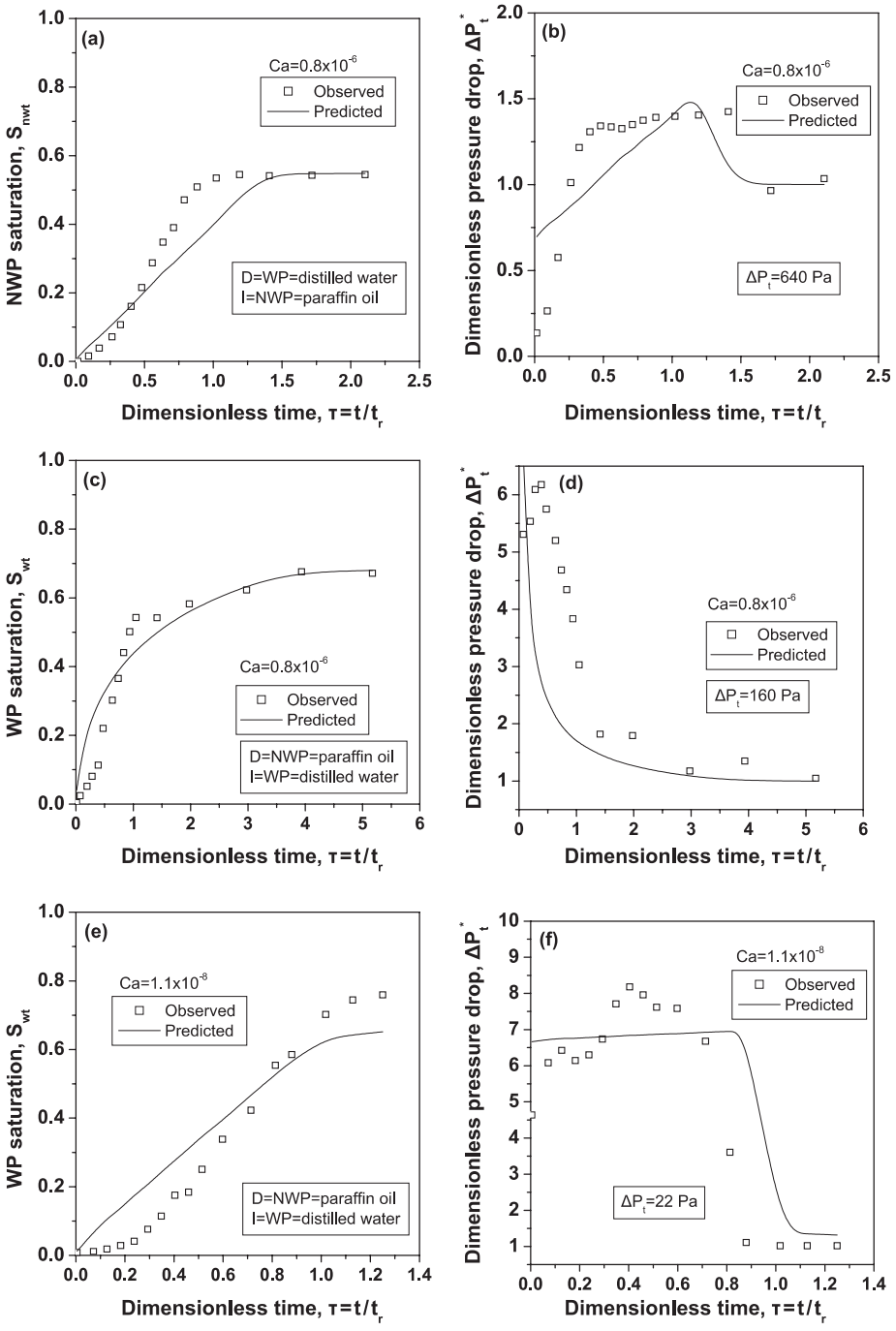

Fig. 13. Comparison of experimentally measured (Fig. 12) with numerically predicted (a) (c) (e) total NWP saturation, and (b) (d) (f) dimensionless total pressure drop, for (a, b) drainage and $Ca = 0.8 \times 10^{-6}$, (c, d) imbibition and $Ca = 0.8 \times 10^{-6}$, and (e, f) imbibition and $Ca = 1.1 \times 10^{-8}$. The parameter values of Table 6 are used.

and b). The relatively high value of the contact angle and the presence of the network of small pores, which preserve the continuity of the NWP, strengthen the compactness of the displacement in imbibition experiments (Fig. 12b and c) so that the measured $S_{wt}(\tau)$ curve is predicted satisfactorily by the numerical simulation (Fig. 13c and e). Regarding the $\Delta P_t^*(\tau)$, the observed discrepancy (Fig. 13d) is reduced at lower *Ca* values (Fig. 13f) as the compactness of the flow pattern is enhanced.

The different growth pattern of drainage and imbibition (Fig. 12a and b) is reflected in the hysteresis between the corresponding k_{rw} and k_{rnw} curves (Fig. 14). On the other hand, both the imbibition k_{rw} and k_{rnw} are increasing functions of *Ca* (Fig. 14, Table 6), exhibiting a behaviour analogous to that observed in model S-1 (Fig. 8, Table 5). The non-equilibrium capillary pressure curve estimated from imbibition experiments is a decreasing function of *Ca* (Table 6) in agreement with Eq. (23).

Capillarity may allow the fast advancement of WP/NWP menisci in small pores before the viscous flow of menisci in large pores bypasses the sub-networks of small pores (Table 2, Fig. 15). At low *Ca* values, the capillary-driven flow of WP in small pores may be so fast that a significant fraction of the sub-networks of small pores are filled with WP before these regions are bypassed by the viscous flow of WP in the network of large pores (Fig. 15a and b). The capillary penetration of WP in small pores combined with the slow displacement of NWP from large pores enhances the hydraulic continuity of the WP so that the efficiency of the displacement increases and the residual NWP decreases with the *Ca* decreasing (Fig. 15a and b). At the network scale, the displacement growth pattern is dominated by viscous fingers (Fig. 15a–c, Table 2). The compactness of the growth pattern is enhanced at low *Ca* values (Fig. 15b) because of the fast capillary flow of WP in small pores (Fig. 15b). In the case that the NWP is a shear-thinning fluid, the viscous fingers are characterized by irregular interfacial configurations (Fig. 15c) caused by the above-mentioned precursor advancement-swelling mechanism.

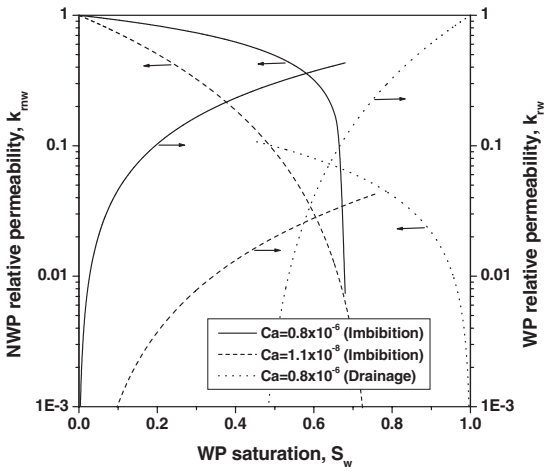

Fig. 14. Drainage and imbibition relative permeability curves of model porous medium D-1 estimated from displacement experiments at two *Ca* values (Fig. 12).

Table 6
Parameters of k_{rw}, k_{rnw}, P_c estimated from displacement experiments performed on model D-1

Displacement	NWP	WP	Ca	P_c^0 (Pa)	m_c (b_c)	k_{rw}^0	m_w (b_w)	k_{rnw}^0	m_{nw} (b_{nw})
Drainage	Paraffin oil with oil red	Distilled water	0.8×10^{-6}	431.3 ± 88.9	0.03 ± 0.0062 (10^{-3})	1.0	2.466 ± 0.0063 (10^{-4})	0.108	0.9414 (10^{-4})
Imbibition	Paraffin oil with oil red	Distilled water	0.8×10^{-6}	3.0	7.8×10^{-4} (10^{-4})	0.431	1.169 (10^{-4})	1.0	0.533 (10^{-4})
Imbibition	Paraffin oil with oil red	Distilled water	1.1×10^{-8}	121.9	9.4×10^{-4} (10^{-4})	0.043	1.833 (10^{-4})	1.0	2.243 (10^{-4})
Imbibition	Paraffin oil	Distilled water with methylene blue	0.8×10^{-6}	3.7	0.037 (10^{-3})	0.222	0.719 (10^{-3})	1.0	1.21 ± 0.517 (10^{-3})
Imbibition	Ozokerite in paraffin oil	Aqueous PEG solution	0.8×10^{-6}	37.9 ± 12.2	0.0 (10^{-4})	0.6125	2.032 ± 0.148 (10^{-4})	1.0	0.204 (10^{-4})

Although both $S_{wt}(\tau)$ and $\Delta P_t^*(\tau)$ are predicted satisfactorily for the case of the Newtonian NWP (Fig. 16a and b) we were unable to fit simultaneously the corresponding transient responses for the case of the shear-thinning NWP (Fig. 16c and d). The strongly nonlinear flow coupled with the dual porosity lead to a highly complicated growth pattern (Fig. 15c) which is difficult to reproduce by using simple relative permeability functions. Probably, the prediction could be improved by using two different relative permeability functions for the two networks.

The permanent retention of the shear-thinning NWP in single pores results in an increase of the hydraulic conductivity and subsequently of the relative permeability of this phase (Fig. 17, Table 6). When the shear-thinning rheology of the NWP strengthens, the WP flows along pore edges rather than at a piston-type fashion, it occupies only a fraction of the cross-section of the large pores, and hence the relative permeability of WP decreases (Fig. 17, Table 6). The capillary forces are more evident when the WP film flows along pore edges, with result that the estimated P_c curve is expected to increase with the NWP shear-thinning rheology strengthening (Table 6). In addition, the increase of P_c^0 (Table 6) is consistent with Eq. (23) and the higher viscosity of WP (Table 2).

4.4. Flow-rate effects on the 2-phase flow coefficients of 3-D porous media

The glass micromodels are small planar pore networks with 2-D topology and relatively narrow capillary-diameter distribution (Tsakiroglou and Payatakes, 1998). On the other hand, porous samples used in core analysis tests (e.g. cores of reservoir rocks or soils) are commonly large 3-D pore networks with broad pore- and throat-size distributions (Tsakiroglou and Payatakes, 2000). In 3-D porous samples, the hydraulic continuity of both phases (bi-continua) is retained over a wide range of fluid saturations, and the linear dimension of the sample may be longer or shorter than the thickness of the unstable and fractal front (e.g. capillary fingering, viscous

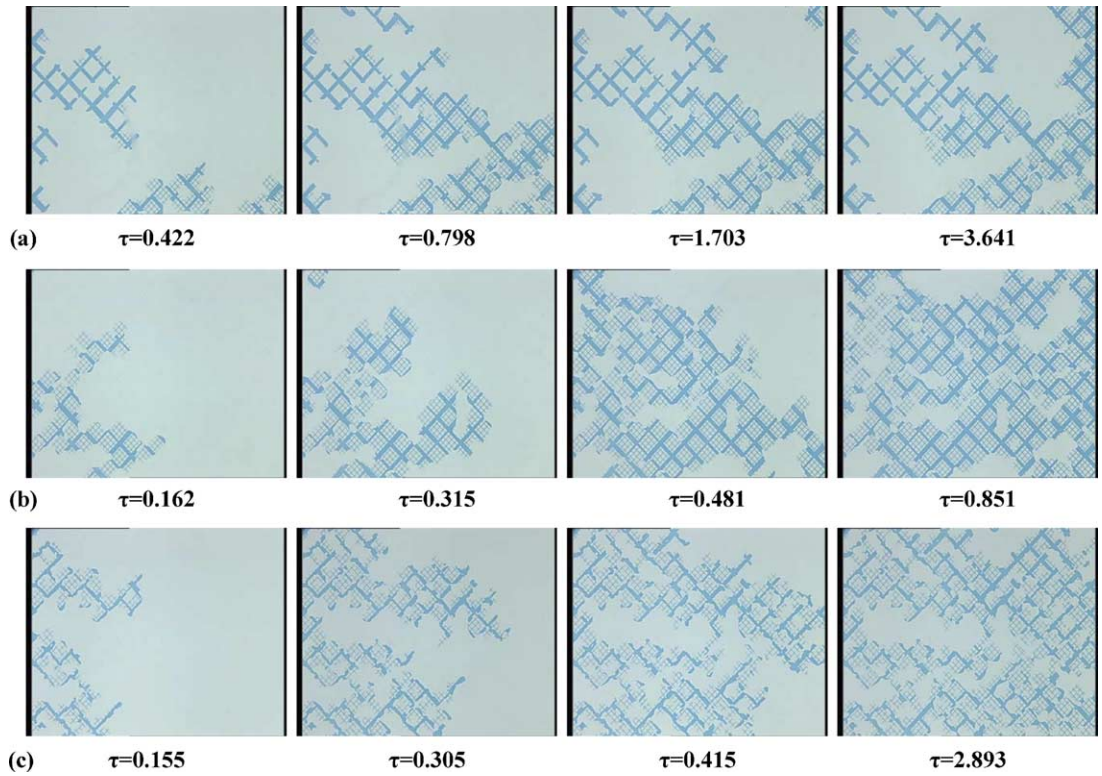

Fig. 15. (a) Imbibition growth pattern in model D-1 where a paraffin oil (Newtonian NWP) is displaced by distilled water coloured with methylene blue (dark) at $Ca = 0.8 \times 10^{-6}$. (b) Imbibition growth pattern in model D-1 where paraffin oil (Newtonian NWP) is displaced by distilled water at $Ca = 10^{-7}$. (c) Imbibition growth pattern in model D-1 where a dispersion of ozokerite ($x_{OZ} = 0.02$) in paraffin oil (shear-thinning NWP) is displaced by an aqueous solution of PEG ($x_{PEG} = 0.055$) at $Ca = 0.8 \times 10^{-6}$.

fingering). Under such conditions, the transient growth pattern may be dominated by a stable frontal drive over a wide range of *Ca* values, compared to 2-D pore systems. Moreover, the high variability of the pore sizes in a 3-D pore system may increase significantly the contribution fraction of the pore size distribution to the dominant displacement pattern. Having realized that the transient displacement pattern is correlated closely with k_{rw} and k_{ro}, the relative permeabilities estimated from displacement experiments performed on planar pore networks may be sensitive to *Ca* over a wider range of *Ca* values compared to the k_{rw} and k_{ro} of 3-D porous samples. Nevertheless, the dependence of the k_{rw} and k_{ro} on the flow rates cannot be overlooked for 3-D pore systems, and must be taken into account in data interpretation.

5. Conclusions

Drainage and imbibition experiments are performed at constant influx rate, on three different model porous media: two simple and one dual pore network. Three fluid systems exhibiting a vari-

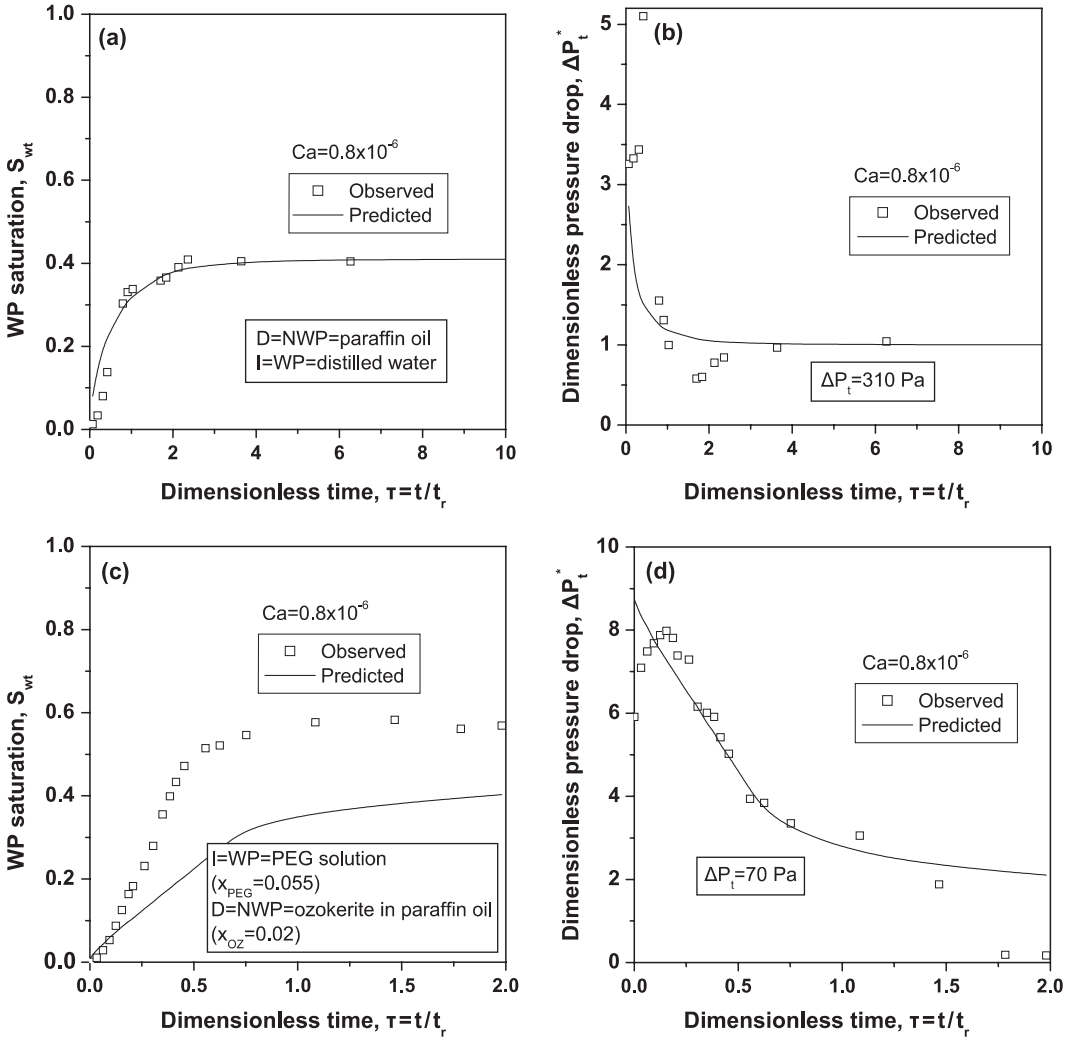

Fig. 16. Comparison of experimentally measured (Fig. 15a and c) with numerically predicted (a) (c) total NWP saturation, and (b) (d) dimensionless total pressure drop, for (a, b) Newtonian NWP and $Ca = 0.8 \times 10^{-6}$, (c, d) shear-thinning NWP and $Ca = 0.8 \times 10^{-6}$. The parameter values of Table 6 are used.

ety of contact angles are used: paraffin oil/water coloured with methylene blue, paraffin oil coloured with oil red/water, and shear-thinning dispersion of ozokerite in paraffin oil/aqueous solution of PEG coloured with methylene blue. The capillary pressure and relative permeability curves are estimated at varying values of the capillary number by using a numerical scheme of inverse modelling to fit the measured transient responses of the total fluid saturation, and pressure drop across the pore network to the numerical solution of PDEs that describe the two-phase flow in porous media.

Except for the capillary number, wettability and viscosity ratio, the displacement growth pattern in a porous medium depends on the fluid rheology and the length scale of the porous sample.

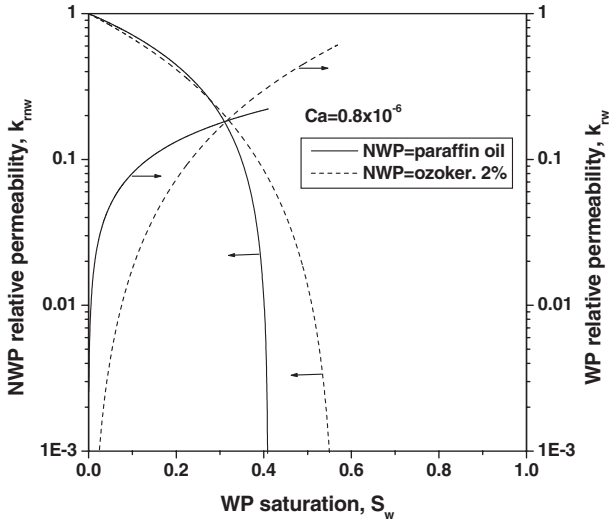

Fig. 17. Imbibition relative permeability curves of model porous medium D-1 estimated from displacement experiments of Newtonian and shear-thinning NWP at one Ca value (Fig. 15a and c).

When the length of the porous sample is smaller than the thickness of the fractal frontal region, then capillary fingers may be evident in a fast and otherwise compact displacement, while a compact pattern may characterize a slow displacement driven by capillarity. When the contact angle is low, and the non-wetting fluid in an imbibition experiment exhibits a pronounced shear-thinning flow behaviour the precursor advancement-swelling mechanism becomes the prevailing one at sufficiently low values of the capillary number; then, the flow pattern is characterized by the coexistence of both fluids and the creation of irregular interfacial configurations in individual pores.

The relative permeability and capillary pressure curves, estimated from transient displacement experiments, are not unique functions of the fluid saturation, but are closely related to the capillary number and subsequently to the dominant flow pattern. The imbibition k_{rnw} increases as the flow pattern changes from compact displacement to viscous fingering or from viscous to capillary fingering. The imbibition k_{rw} increases as the flow pattern changes from compact displacement or capillary fingering to viscous fingering. As the shear-thinning behaviour of the NWP strengthens and/or the contact angle decreases, then the flow pattern is gradually dominated by irregular configurations, and the imbibition k_{rnw} increases. The imbibition P_{c} is an decreasing function of Ca or increasing function of μ_{I} in agreement with the linear thermodynamic theory.

Acknowledgement

This work was performed under Energy Environment and Sustainable Development (EESD) contract number EVK1-CT1999-00013 (project acronym: TRACe-Fracture) supported by the European Commission.

Appendix A. Transport properties of dual pore networks

The dual pore network D-1 is created by the superposition of a network of narrow and short pores of length l_n and permeability k_n upon a network of wide and long pores of length l_w and permeability k_w. The total volumetric rate flowing through a cross-sectional area of the network can be regarded equal to the sum of the rates flowing through the two sub-networks. Then it results that the total permeability is given by

$$k = k_n + \left(\frac{l_w}{l_n}\right) k_w. \tag{A.1}$$

Regarding the single-phase flow of a shear-thinning NWP through the dual pore network, the flow balance leads to the relation

$$\frac{k'}{\langle \mu_{nw} \rangle} = \frac{k'_n}{\langle \mu_{nw} \rangle_n} + \left(\frac{l_w}{l_n}\right) \frac{k'_w}{\langle \mu_{nw} \rangle_w}, \tag{A.2}$$

where the effective permeabilities k'_n, k'_w, and average viscosities $\langle \mu_{nw} \rangle_n$, $\langle \mu_{nw} \rangle_w$ are calculated separately on each sub-network (Tsakiroglou, 2002; Tsakiroglou et al., 2005). Eq. A.2 allows us to determine the effective properties of the dual pore network from properties of the constituent sub-networks.

References

Aker, E., Maloy, K.J., Hansen, A., Batrouni, G.G., 1998. A two-dimensional network simulator for two-phase flow in porous media. Transp. Porous Media 32, 163–186.

Bear, J., 1972. Dynamics of Fluids in Porous Media. Elsevier, New York.

Birovljev, A., Furuberg, L., Feder, J., Jossang, T., Maloy, K.J., Aharony, A., 1991. Gravity invasion percolation in two dimensions: experiment and simulation. Phys. Rev. Lett. 67, 584–587.

Blunt, M., King, P., 1991. Relative permeabilities from two- and three-dimensional pore-scale network modelling. Transp. Porous Media 6, 407–433.

Cieplak, M., Robbins, M.O., 1990. Influence of contact angle on quasistatic fluid invasion of porous media. Phys. Rev. B 41, 11508–11521.

Constantinides, G.N., Payatakes, A.C., 2000. Effects of precursor wetting films in immiscible displacement through porous media. Transp. Porous Media 38, 291–317.

Dias, M.M., Payatakes, A.C., 1986a. Network models for two-phase flow in porous media. Part I. Immiscible microdisplacement of non-wetting fluids. J. Fluid Mech. 164, 305–336.

Dias, M.M., Payatakes, A.C., 1986b. Network models for two-phase flow in porous media. Part II. Motion of oil ganglia. J. Fluid Mech. 164, 337–358.

Ferer, M., Sams, W.N., Geisbrecht, R.A., Smith, D.H., 1993. Crossover from fractal to compact flow from simulations of two-phase flow with finite viscosity ratio in two-dimensional porous media. Phys. Rev. E 47, 2713–2723.

Ferer, M., Sams, W.N., Geisbrecht, R.A., Smith, D.H., 1995. Fractal nature of viscous fingering in two-dimensional pore level models. AIChE J. 41, 749–763.

Ferer, M., Bromhal, G.S., Smith, D.H., 2003. Pore-level modeling of immiscible drainage: validation in the invasion percolation and DLA limits. Physica A 319, 11–35.

Gouyet, J.-F., Rosso, M., Sapoval, B., 1988. Fractal structure of diffusion and invasion fronts in three-dimensional lattices through the gradient percolation approach. Phys. Rev. B 37, 1832–1838.

Hassanissadeh, S.M., Celia, M.A., Dahle, H.K., 2002. Dynamic effect in the capillary pressure–saturation relationship and its impacts on unsaturated flow. Vadose Zone J. 1, 38–57.

Huang, D.D., Honarpour, M.M., 1998. Capillary end effects in coreflood calculations. J. Pet. Sci. Eng. 19, 103–117.
Hughes, R.G., Blunt, M.J., 2000. Pore scale modeling of rate effects in imbibition. Transp. Porous Media 40, 295–322.
Kulkarni, R., Watson, A.T., Norttvedt, J.-E., Sylte, A., 1998. Two-phase flow in porous media: property identification and model validation. AIChE J. 44, 2337–2350.
Lenormand, R., Touboul, E., Zarcone, C., 1988. Numerical models and experiments on immiscible displacement in porous media. J. Fluid Mech. 189, 165–187.
Mejia, G.M., Mohanty, K.K., Watson, A.T., 1995. Use of in situ saturation data in estimation of two-phase flow functions in porous media. J. Pet. Sci. Eng. 12, 233–245.
Mitlin, V., Lawton, B., Owen, L., 1999. A semi-analytical procedure for estimating relative permeability from displacement experiments: account for pre-breakthrough data. Int. J. Eng. Sci. 37, 1051–1067.
Sahimi, M., 1995. Flow and Transport in Porous Media and Fractured Rock: From Classical Methods to Modern Approaches. VCH, Weinheim, Germany.
Singh, M., Mohanty, K.K., 2003. Dynamic modelling of drainage through three-dimensional porous materials. Chem. Eng. Sci. 58, 1–18.
Theodoropoulou, M., Karoutsos, V., Tsakiroglou, C., 2001. Investigation of the contamination of fractured formations by non-Newtonian oil pollutants. J. Environ. Forensics 2, 321–334.
Toth, J., Bodi, T., Szucs, P., Civan, F., 2002. Convenient formulae for determination of relative permeability from unsteady-state fluid displacements in core plugs. J. Pet. Sci. Eng. 36, 33–44.
Tsakiroglou, C.D., 2002. A methodology for the derivation of non-Darcian models for the flow of generalized Newtonian fluids in porous media. J. Non-Newtonian Fluid Mech. 105, 79–110.
Tsakiroglou, C.D., 2004. Correlation of the two-phase flow coefficients of porous media with the rheology of shear-thinning fluids. J. Non-Newtonian Fluid Mech. 117, 1–23.
Tsakiroglou, C.D., Payatakes, A.C., 1998. Mercury intrusion and retraction in model porous media. Adv. Colloid Interf. Sci. 75, 215–253.
Tsakiroglou, C.D., Payatakes, A.C., 2000. Characterization of the pore structure of reservoir rocks with the aid of serial sectioning analysis, mercury porosimetry and network simulation. Adv. Water Resour. 23, 773–789.
Tsakiroglou, C.D., Theodoropoulou, M., Karoutsos, V., 2003a. Non-equilibrium capillary pressure and relative permeability curves of porous media. AIChE J. 49, 2472–2486.
Tsakiroglou, C.D., Theodoropoulou, M., Karoutsos, V., Papanicolaou, D., Sygouni, V., 2003b. Experimental study of the immiscible displecement of shear-thinning fluids in pore networks. J. Colloid Interf. Sci. 267, 217–232.
Tsakiroglou, C.D., Theodoropoulou, M.A., Karoutsos, V., Papanicolaou, D., 2005. Determination of the effective transport coefficients of pore networks from transient immiscible and miscible displacement experiments. Water Resour. Res. 41 (2), W02014.
Tzimas, G.C., Matsuura, T., Avraam, D.G., Van der Brugghen, W., Constantinides, G.N., Payatakes, A.C., 1997. The combined effect of the viscosity ratio and the wettability during forced imbibition through nonplanar porous media. J. Colloid Interf. Sci. 189, 27–36.
Vizika, O., Avraam, D.G., Payatakes, A.C., 1994. On the role of the viscosity ratio during low-capillary number forced imbibition in porous media. J. Colloid Interf. Sci. 165, 386–401.
Whitaker, S., 1986. Flow in porous media II: The governing equations for immiscible, two-phase flow. Transp. Porous Media 1, 105–125.
Wilkinson, D., 1986. Percolation effects in immiscible displacement. Phys. Rev. A 34, 1380–1391.
Xu, B., Salin, D., Yortsos, Y.C., 1998. Invasion percolation with viscous forces. Phys. Rev. E 57, 739–751.
Zhang, J-H., Liu, Z-H., 1998. Study of the relationship between fractal dimension and viscosity ratio for viscous fingering with a modified DLA model. J. Pet. Sci. Eng. 21, 123–128.